Capillarity

Vol. 3, No. 1, p. 8-15, 2020

Original artical

Capillary imbibition of confined water in nanopores

Fanhui Zeng[1]*, Qiang Zhang[1], Jianchun Guo[1], Yong Meng[2], Xianzhen Shao[2], Yingjie Zheng[2]

[1]*State Key Laboratory of Oil and Gas Reservoir Geology and Exploitation, Southwest Petroleum University, Chengdu 610500, P. R. China*

[2]*Hekou Oil Production Plant, Shengli Oil Field, Dongying 257200, P. R. China*

Keywords:
Shale gas formation
nanopore confined flow
slippage
wettability
viscosity
spontaneous imbibition

Cited as:
Zeng, F., Zhang, Q., Guo, J., Meng, Y., Shao, X., Zheng, Y. Capillary imbibition of confined water in nanopores. *Capillarity*, 2020, 3(1): 8-15, doi: 10.26804/capi.2020.01.02.

Abstract:
The spontaneous capillary imbibition of confined nanopores is investigated using an analytical model that includes the slip effect, wettability and effective viscosity at the water surface interface. The results show that the effective viscosity of confined water is larger than that of bulk water and decreases with diameter and wettability. The effective slip length is negative for a contact angle of 0°, and the effective slip length is positive and increases with diameter. The results of the presented model show that the capillary imbibition length for nanoconfined water can vary up to 0.389-1.033 times that determined by the Lucas-Washburn equation with no-slip boundary conditions for nanopores due to the effective viscosity and slippage with various dimensions and contact angles. The enhancement increases with diameter and contact angle. These results elucidate the confined movement through nanopores, which can be used to understand fracturing-fluid flow in the nanopores of shale reservoir formations.

1. Introduction

Capillary-dominated Shale formations typically have very small nanoscale channels (Cipolla, 2009; Loucks et al., 2012; Wang and Rahman, 2016), and horizontal well drilling accompanied by multistage slickwater fracturing is the key technology unlocking shale gas resources (Zeng and Guo, 2016; Zeng et al., 2018). The backflow of fracturing fluid is the last step in the hydraulic fracturing process, and several investigators have pointed out that less than 50% of the injected fracturing fluid can be recovered (Alkouh, 2014; Ghanbari and Dehghanpour, 2016). The remaining water is trapped in the fracture network and taken up into the confined nanopores through spontaneous imbibition, which is regarded as the main cause of low water recovery (Abgrall and Nguyen, 2008; Birdsell et al., 2015; Falk et al., 2014). Improving our understanding of the fluid flow behavior in nanoscale pores is critical to optimizing shale gas recovery in unconventional reservoirs (Akbarabadi et al., 2017).

Due to the importance of spontaneous imbibition (SI) in many practical problems, several investigators have carefully addressed this phenomenon. Lucas-Washburn (LW) (Lucas, 1918; Washburn, 1921) established the classical SI solution for the capillary-driven penetration of liquids into uniform cross-section curl capillary tubes. Several investigators applied the LW equation to investigate water imbibition directly (Benavente et al., 2002; Yang et al., 2004; Wang and Rahman, 2016). For practical purposes, a geometry correction factor is incorporated for the fluid imbibed by noncylindrical capillaries and the capillary radius is replaced with an effective capillary radius in the LW equation (Benavente et al., 2002; Mortensen et al., 2005; Cai et al., 2012). Overall, these investigations provide deep insights into the fluid complex flow phenomena of macropores.

However, the aforementioned research is based on fundamental assumptions of continuum fluid mechanics and no-slip boundary conditions during fluid dynamic flow (Yang et al., 2004). When fluid flow is scaled down to the nanopore size, fluid-surface interactions lead to a velocity “jump” at the walls (Müller et al., 2008; Sedghi et al., 2014). In the nanoscale pores of shale, it is evident that the boundary condition without the slip effect is no longer valid (Cottin-Bizonne et al., 2003; Holt et al., 2006). Furthermore, the confined water flow exhibits a dramatic change in viscosity compared with that of bulk water (Li et al., 2007). The confined water effective viscosity in the wall area is larger than that of bulk water (Feibelman, 2013) in hydrophilic nanopores because

*Corresponding author.
E-mail address: zengfanhui023024@126.com (F. Zeng); zq1819096@163.com (Q. Zhang); guojianchun@vip.163.com (J. Guo); mengyong682.slyt@sinopec.com (Y. Meng); shaoxianzhen.slyt@sinopec.com (X. Shao); zhengyingjie.slyt@sinopec.com (Y. Zheng).

Received February 21, 2020; revised March 3, 2020; accepted March 4, 2020; available online March 9, 2020.

Ausasia Science and Technology Press

substantial water epitaxial ordering is induced and some fluid layers adhere onto the walls (Thompson and Robbins, 1990). For confined water flow in hydrophobic nanopores, water molecules can effectively slide on the walls (Vinogradova et al., 2009), and the no-slip boundary assumption breaks down (Wu et al., 2017). Furthermore, the confined water flow behavior is mainly determined by the water and nanopore wall interactions, which are substantially different from those in microscale pore flow (Nair et al., 2012; Lorenz and Zewail, 2014). The water/wall interaction occurs at the molecular level and can be represented by true slip, while water intermolecular interactions due to water/water interfaces result from water near the walls, and varying viscosities can be expressed by the apparent viscosity (Wu et al., 2017).

Fortunately, for similar primary flow mechanisms in nanoscale and microscale channels, the continuum fluid mechanics description is still valid for modeling confined water flow in nanopores (Thomas and Mcgaughey, 2009) by modifying the fluid-wall interactive effect (Falk et al., 2014), including different boundary conditions (Heinbuch and Fischer, 1989; Müller et al., 2008; Thomas and Mcgaughey, 2008b) and the dramatic variation in effective viscosity caused by the water and nanopore wall interaction (Klein and Kumacheva, 1995; Scatena et al., 2001; Abgrall and Nguyen, 2008).

A comprehensive literature survey was performed for investigations of fluid transport mechanisms (Zhang et al., 1996; Benavente et al., 2002; Cai et al., 2014; Schmid et al., 2016; Zhang and Sheng, 2017; Xiao et al., 2018). To the best of our knowledge, however, no study has focused on simultaneously incorporating the slip effect, wettability, viscosity and pore size to study the mechanisms of nanofluid spontaneous imbibition at the nanoscale. Here, we present an analytical model for confined water imbibition in nanopores that simultaneously considers the boundary slip, wettability, effective viscosity, nanopore dimension and capillary force. This model can be used to quantitatively describe the imbibition length of confined water, which provides a useful approach for modeling confined water flow in the nanopores of shale formations.

2. Mathematical models

2.1 Hagen-Poiseuille flow equations

The capillary model is applied to simulate the water imbibed in matrix pores during shale formation hydraulic fracturing treatment as shown in Fig. 1.

The driving process of SI is determined by the surface energy and resisted by viscous forces. The ultralow permeability and water uptake by shale formations are quite slow; therefore, inertial forces can be neglected, which reduces the N-S to the Stokes equation (Wang and Rahman, 2016). Considering the no-slip boundary conditions and the steady-state incompressible and laminar flow situation, the velocity profile in a capillary with radius r can be written as follows (Benavente et al., 2002):

$$\frac{\mu}{r}\left[\frac{d}{dr}\left(r\frac{du}{dr}\right)\right]=\frac{dp}{dx} \tag{1}$$

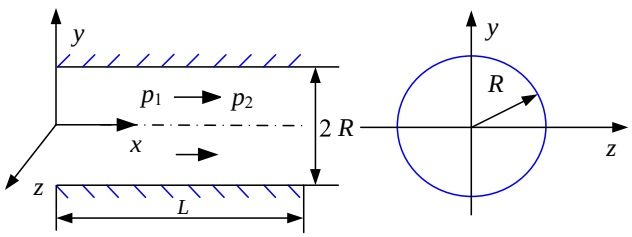

Fig. 1. Laminar flow in a circular tube schematic diagram.

where μ is the fluid viscosity, mPa·s; r is the distance measured from an arbitrary point along the radius of the circular capillary to the capillary center, m; u is the incompressible fluid flow velocity, m/s; and dp/dx is the pressure gradient along the capillary, MPa/m.

Rearranging Eq. (1) can obtain the following:

$$\frac{d^2u}{dr^2}+\frac{1}{r}\frac{du}{dr}-\frac{1}{\mu}\frac{dp}{dx}=0 \tag{2}$$

By integrating Eq. (1), the following can be obtained:

$$u=\frac{1}{4\mu}\frac{dp}{dx}r^2+A\ln r+B \tag{3}$$

where A and B are dimensionless intermediate variables.

The maximum velocity is at the center of the circle, while the velocity gradient is 0. When the fluid is subjected to a no-slip condition at the boundary, the boundary conditions can be expressed as Eq. (4):

$$\begin{cases} r=0, \frac{du}{dr}=0 \\ r=R, u=0 \end{cases} \tag{4}$$

where R is the capillary radius, m.

Inserting Eq. (4) into Eq. (3), the circular capillary velocity distribution can be written as follows:

$$u=\frac{1}{4\mu}\frac{\Delta p}{L}(R^2-r^2) \tag{5}$$

where Δp is the pressure drop along the capillary, MPa; and L is the capillary tube length, m.

The flux is obtained by integrating the velocity distribution over the flow area:

$$q=\int_0^R \frac{1}{4\mu}\frac{\Delta p}{L}(R^2-r^2)2\pi r dr=\frac{\pi R^4}{8\mu}\frac{\Delta p}{L}=\frac{\pi d^4}{128\mu}\frac{\Delta p}{L} \tag{6}$$

where q is the flux rate, m^3/s; d is the circular capillary diameter, m; and $d = 2R$.

Eq. (6) is the Hagen-Poiseuille flow equation, which is valid for a straight capillary tube of circular cross-section under no-slip boundary conditions.

The average velocity in a circular capillary can be written as follows:

$$\bar{u}=\frac{q}{\pi R^2}=\frac{R^2}{8\mu}\frac{\Delta p}{L} \tag{7}$$

where $\bar{u}$ is the incompressible fluid average velocity, m/s.

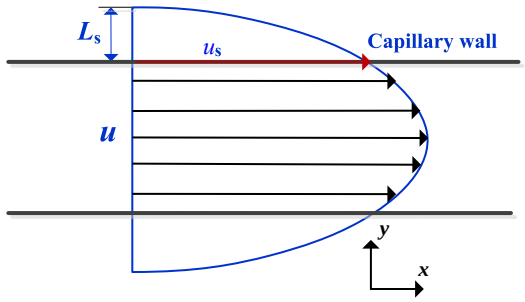

Fig. 2. Schematic diagram of the slip length correction in the external boundary condition.

2.2 Hagen-Poiseuille flow equation with the slip effect

The slip effect that exists at walls can have important implications on the boundary layer flow in fluid mechanics (Voronov et al., 2006). When the confined fluid flow occurs in nano-capillary channels, the continuum fluid mechanics description in the Navier-Stokes Eq. (1) is still valid, while the external boundary conditions in Eq. (4) should be modified by Navier boundary conditions (Kalyon, 2005; Dimitrov et al., 2007; Thomas and Mcgaughey, 2008b; Ortiz-Young et al., 2013), and they are characterized by the slip length L_s shown in Fig. 2. The modified boundary conditions are expressed in Eq. (8).

$$\begin{cases} r=0, \frac{du}{dr}(r=R+L_s)=0 \\ r=R, u_s=-L_s\frac{\partial u}{\partial r}\mid_{r=R} \end{cases} \tag{8}$$

where L_s is the fluid slip length at the liquid/solid boundary, m.

Inserting Eq. (8) into Eq. (3), the velocity distribution equation is obtained:

$$u=\frac{1}{4\mu}\frac{dp}{dx}(r^2-R^2-2RL_s)=\frac{1}{4\mu}\frac{\Delta p}{L}(R^2+2RL_s-r^2) \tag{9}$$

Integrating Eq. (9), we obtain the flow flux considering the slip effect.

$$\begin{aligned} q&=\int_0^R\frac{1}{4\mu}\frac{\Delta p}{L}(R^2+2RL_s-r^2)2\pi r dr \\ &=\frac{\pi R^4}{8\mu}\frac{\Delta p}{L}\left(1+\frac{4L_s}{R}\right)=\frac{\pi d^4}{128\mu}\frac{\Delta p}{L}\left(1+\frac{4L_s}{R}\right) \end{aligned} \tag{10}$$

Eq. (10) is the slip-modified Hagen-Poiseuille flow rate formula, which is in accordance with the formula derived by Holt et al (2006). By setting L_s = 0, the no-slip condition Hagen-Poiseuille flow rate equation can be obtained (Salwen et al., 1980; Cai et al., 2014).

The average velocity in a circular capillary that considers the slip can be written as follows:

$$\bar{u}=\frac{q}{\pi R^2}=\frac{R^2}{8\mu}\frac{\Delta p}{L}\left(1+\frac{4L_s}{R}\right) \tag{11}$$

When setting L_s to zero, Eq. (11) can be reduced to the average velocity of the incompressible fluid in the capillary without the slip length effect as shown in Eq. (7).

For fluid flow in confined nanopores, the fluid properties are influenced by the fluid/fluid and wall/fluid interactions at the wall boundary. Hence, a precise description of the phenomena taking place at these interfaces becomes important (Sofos et al., 2012). Here, we focused on addressing the determination of the effective slippage length and the confined nanochannel fluid viscosity.

2.2.1 Effective slippage length determination

Confined channel liquid-wall interactions are strongly influenced by the stationary solid surface morphology and physical and chemical features (Cottinbizonne et al., 2003), which are determined by the boundary wall wettability at low shear rates (Maali et al., 2008). True slip represents fluid molecules effectively sliding on walls, which occurs at a molecular level and can be calculated by the contact angle for a given liquid under given conditions (Granick et al., 2003; Huang et al., 2008).

$$L_s=\frac{C}{(\cos\theta+1)^2} \tag{12}$$

where C is a constant, m, which is 0.41 as determined by a molecular dynamics (MD) simulation (Huang et al., 2008); and θ is the contact angle, °.

The viscosity of confined water near walls varies dramatically from that of bulk water, which induces apparent slip at water/water interfaces (R. Jay Mashl et al., 2015). For real applications, the confined fluid slip length considering true and apparent slip effects should be replaced by the effective slip length L_{se} (Wu et al., 2017).

$$L_{se}=L_{sa}+L_s=\left(\frac{\mu_\infty}{\mu_d}-1\right)\left(\frac{d}{8}+L_s\right)+L_s \tag{13}$$

where L_{se} is the effective slip length, m; L_{sa} is the apparent slip length, m; μ_∞ is the bulk fluid viscosity, Pa·s; and μ_d is the confined fluid effective viscosity, Pa·s.

Eq. (13) shows that the effective slip length relies on the wall wettability, fluid viscosity, and capillary dimension (Thomas and Mcgaughey, 2008b).

2.2.2 Confined nanofluid flow viscosity

When confined liquid flows in nano-sized pores, the fluid viscosity near the pore wall is no longer accurately described by the core flow fluid viscosity (Fradin et al., 2000; Bocquet and Tabeling, 2014). The effective viscosity is determined by the viscosity of the core flow fluid and interface area, which can be written as follows (Thomas and Mcgaughey, 2008b; Shaat, 2017):

$$\mu_d=\mu_i\frac{A_{id}}{A_{td}}+\mu_\infty\left(1-\frac{A_{id}}{A_{td}}\right) \tag{14}$$

where μ_i is the fluid viscosity in the interface region, Pa·s; A_{id} is the area of the interface region, m^2, $A_{id}=\pi[(d/2)^2-(d/2-$

$d_c)^2]$; d_c is the confined fluid critical thickness, m, for which the value can be set as 0.7 nm on the basis of experiments and MD simulations (Werder et al., 2001; Thomas and Mcgaughey, 2008a); μ_∞ is the bulk fluid viscosity, Pa·s; and A_{td} is the total cross-sectional area, m^2, $A_{td} = \pi(d/2)^2$.

The interface region water viscosity is also strongly influenced by the fluid-wall interaction, which can be represented as follows (Raviv et al., 2001):

$$\frac{\mu_i}{\mu_\infty} = -0.018\theta + 3.25 \tag{15}$$

From Eq. (15), it is clear that the interface region fluid viscosity varies dramatically with the contact angle (Petravic and Harrowell, 2009; Haria et al., 2012). Eq. (16) is applied to determine the bulk water viscosity (Laliberté, 2007), which is valid for temperatures from 273.15 K to 423.15 K (Herington, 1977).

$$\mu_\infty = \frac{(T-273.15)+246}{[0.05594(T-273.15)+5.842](T-273.15)+137.37} \tag{16}$$

where T is the temperature of bulk water, K.

2.2.3 Capillary SI equation

(1) Capillary force

For a circular capillary tube, the Young-Laplace equation is used to determine the capillary pressure, which is also validated and applicable to a nano capillary (Liu and Cao, 2016), such as in Eq. (17):

$$p_c = \frac{4\sigma\cos\theta}{d} \tag{17}$$

where p_c is the capillary pressure, Pa; σ is the liquid-gas interface surface tension, N/m.

Considering that the capillary pressure is the only SI pressure, inserting Eqs. (13)-(17) into Eq. (10) yields the SI flow rate equation under the influence of slip, effective viscosity and capillary force.

$$\begin{aligned} q_s &= \int_0^r \frac{1}{4\mu_d}\frac{\Delta p}{L}(R^2+2RL_{se}-r^2)2\pi r dr \\ &= \frac{\pi d^3}{32\mu_d}\frac{\sigma\cos\theta}{L}\left(1+\frac{4L_{se}}{R}\right) \end{aligned} \tag{18}$$

where q_s is the capillary flow rate considering the slippage effect and the effective viscosity, m^3/s.

(2) SI length equation under capillary force

In view of the material balance principle, the flow rate must equal the rate of the total pore volume imbibed (Washburn, 1921; Benavente et al., 2002; Cai et al., 2014).

$$q_s = \frac{\pi d^2}{4}\frac{dL}{dt} \tag{19}$$

where t is the imbibition time, min.

Considering that Eq. (19) equals Eq. (18), the time parameter is integrated and substituted into the boundary condition, so that when t = 0, L = 0. The circular capillary spontaneous length can be obtained:

$$L_{sed} = \sqrt{\frac{d\sigma\cos\theta}{4\mu_d}\left(1+\frac{8L_{se}}{d}\right)}\sqrt{t} \tag{20}$$

where L_{sed} is the capillary imbibition length with time considering the slippage effect and effective viscosity, m.

The SI model presented in Eq. (20) is sufficiently general, which considers the slip effect and effective viscosity at the same time.

3. Model validation and application

3.1 Comparison with the LW equation

Under the assumption of the no-slip boundary condition, Washburn (1921) applied Poiseuille's law to derive the following:

$$L_\infty = \sqrt{\frac{d\sigma\cos\theta}{4\mu_\infty}}\sqrt{t} \tag{21}$$

where L_∞ is the fluid SI length, m.

Eq. (21) is a special case of Eq. (20), setting L_{se} = 0, μ_d = μ_∞, and Eq. (20) reduces to the LW model.

Dividing Eq. (20) by Eq. (21) gives the capillary spontaneous length increment considering the slip and effective viscosity.

$$\varepsilon = \frac{L_{sed}}{L_\infty} = \sqrt{\frac{\mu_\infty}{\mu_d}\left(1+\frac{8L_{se}}{d}\right)} \tag{22}$$

Eq. (22) shows the high sensitivity of ε to μ_d and L_{se}.

3.2 Model application

Most shale gas formations are completely hydrophilic or partially hydrophilic (Ruppert et al., 2013); hence, we choose contact angles that vary within the range of 0° to 90°. The other basic calculation factors are as follows: T = 25 °C, d_c = 0.7 nm, C = 0.41, σ = 50 mN/m and imbibition time = 60 min.

Fig. 3 shows the plots of effective viscosity and bulk viscosity versus pore diameters ranging from 2 nm to 20 nm under different contact angles. The value of the water effective viscosity is always larger than that of bulk water. The bulk viscosity is clearly independent of diameter, while the effective viscosity decreases dramatically with diameter to coincide with the bulk fluid viscosity. Our results agree with those of Shah (Shah, 2010), who found that the water viscosity in a 2 nm diameter capillary under a contact angle of 0° is elevated by approximately 205% and the enhancement decreases rapidly as the pore size increases. Shah attributed the enhanced apparent viscosity to an increase in the ordering of polar water molecules near the pore wall where a highly viscous boundary layer exists (Shah, 2010).

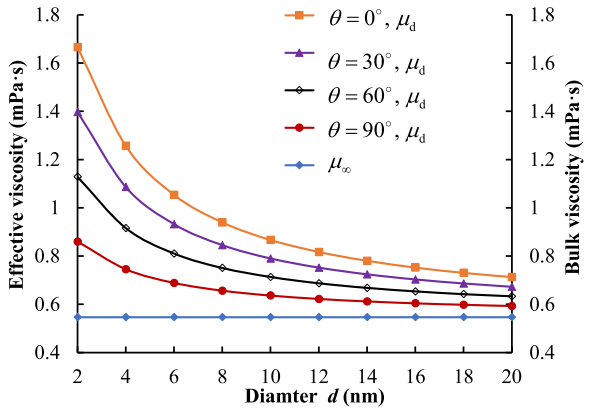

Fig. 3. Effective viscosity and bulk viscosity versus pore diameter.

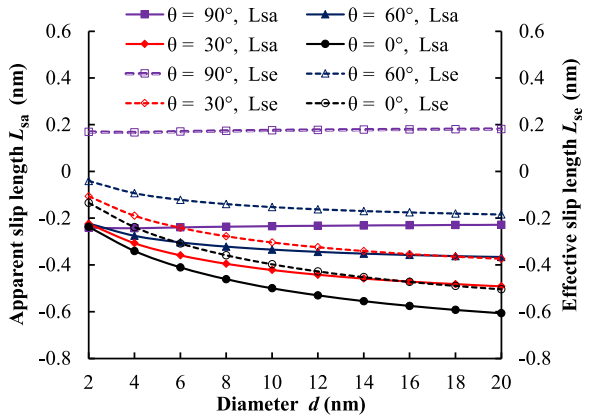

Fig. 4. Apparent/effective slip length variation with diameter for different contact angles.

Although these interactions exist in large pores, they have little influence on the fluid properties. The reason is that for confined water, the effective viscosity is determined by a weighted average of the bulk water and the interface water viscosity; hence, the effective viscosities are lower than those of narrow pores because more fluid molecules exist in the wider pore central region, resulting in a substantially decreased viscosity (Shaat, 2017).

Furthermore, a dramatic variance in the effective viscosity is observed for different contact angles, especially for smaller pore sizes, which comprehensively reflects the fluid and fluid-wall interactive effects. Due to the high effective viscosity for the smaller contact angle due to the more hydrophilic capillary, the fluid contact layer behaves as a solid layer (Din and Michaelides, 1997).

The slip length has a profound effect on the confined imbibition in nanoscale pores; therefore, precise quantification of the fluid slip effect becomes very important. There are three different slip lengths that reflect the water-wall interaction (true slip L_s), the water-water interaction (apparent slip L_{sa}) and the interactions between the former two (effective slip L_{se}).

Fig. 4 shows that the L_{se}. value varies with the contact angle for different diameters. Experimental studies revealed

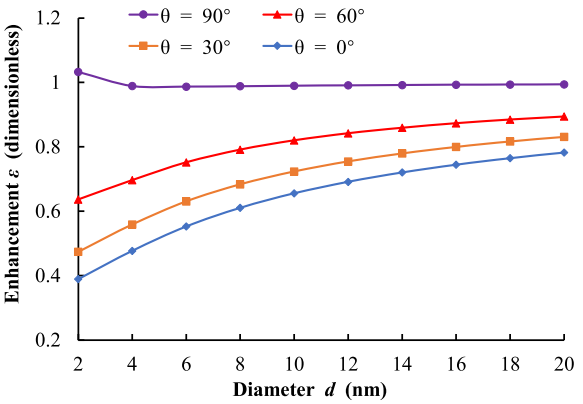

Fig. 5. Enhancement ε variation with diameter for different contact angles.

that the near-wall fluid density is oscillatory and that the maximum local density is affected by the wall-fluid interaction potential (Chan and Horn, 1985). As a result, several molecular layers are adsorbed and fixed on the solid surface. Under the strong wall-fluid interaction (for a small contact angle), the effective boundary is located at the high viscosity region edge (Din and Michaelides, 1997), implying that immobile layers exist at the wall (Chan and Horn, 1985). The relation decreases as the contact angle increases.

Fig. 4 also reveals that the effective slip increases as the contact angle increases because the interaction strength of the fluid atoms is stronger than the fluid-wall effect, which causes the fluid to recede from the wall and results in a greater slip length, which enhances the slip effect (Kannam et al., 2011).

Fig. 5 shows the imbibition length enhancement ε versus nanopore diameter for the ten studied diameters. For comparison, we also provide the enhancement corresponding to different contact angles. The enhancement ε varies dramatically for smaller nanopores than for larger nanopores, where large surface effects and slip length effects reduce the imbibition length. For larger diameters, the core fluid area increases and the enhancement factor varies more smoothly than for smaller diameters.

A relatively small decrease in the enhancement ε from 0.994-1.033 can occur for water confined in nanopores with a contact angle of 90° due to the smaller interactive influence than at other contact angles, which has been validated by many investigators (Granick, 1991; Thompson and Troian, 1997). For contact angles of 0°, 30° and 60°, the enhancement ε increased by a factor of 0.389-0.894 as the diameter increased from 2 to 20 nm. These differences may arise from the water and nanopore wall interaction strength, which is determined by the water-wall contact angle (Voronov et al., 2006; Shannon et al., 2008).

3.2.1 Imbibition length variation with pore size for different imbibition times

Fig. 6 shows the imbibition length L of moving water as a function of $t^{1/2}$ for the four diameters of 20 nm, 14 nm, 8 nm and 2 nm. There is a perfect linear relation between L and $t^{1/2}$, and the slopes of the lines are 0.4052, 0.318, 0.2108 and

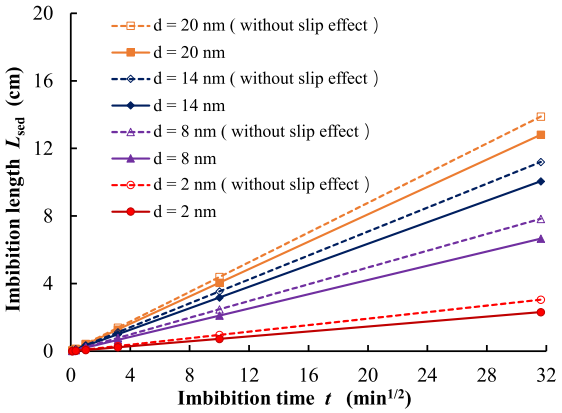

Fig. 6. Imbibition length versus the square root of time for different pore sizes with θ = 30°.

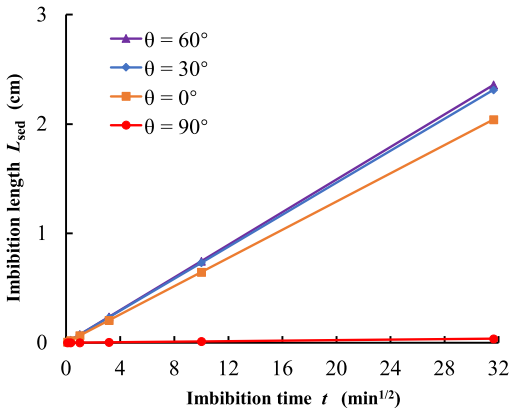

Fig. 7. Imbibition length versus the square root of time for different contact angles with d = 2 nm.

0.0731 for pore diameters of 20 nm, 14 nm, 8 nm and 2 nm, respectively. The plotted lines imply that the imbibition length increases as the diameter increases, meaning that during shale gas hydraulic fracturing, the water imbeds into larger pores more easily than into smaller pores, which is validated by a previous study (Hsu et al., 2014). Fig. 6 also reveals that the imbibition length would decrease when slip effect is considered, which is consistent with Fig. 4.

3.2.2 Imbibition length variation with contact angle for different imbibition times

Fig. 7 shows the imbibition length L of moving water as a function of $t^{1/2}$ for contact angles of 0°, 30°, 60°, and 90°. There is a perfect linear relation between L and $t^{1/2}$, and the slopes of the lines are 0.0645, 0.0731, 0.0746 and 0.0012 for contact angles of 60°, 30°, 0° and 90°, respectively. The plotted lines imply that the imbibition length was comprehensively influenced by the slip effect and capillary pressure. A smaller contact angle implies that the liquid molecules adhere to the wall, while a larger capillary pressure is the dominant influence on the imbibition length. Compared to the results in Fig. 6, the pore size has a profound effect on the imbibition length.

4. Conclusions

(1) Spontaneous imbibition is an important component in studying shale formation hydraulic fracturing. The relative contribution of the effective viscosity and slip length during the imbibition phenomenon needs to be considered during this process. The interrelationships among the viscosity of nanoconfined water, the interface slippage and the wettability of the confining surfaces were carefully investigated.

(2) The results of the presented model show that the capillary imbibition length of nanoconfined water can vary up to 0.389-1.033 times that determined by the LW equation with no-slip boundary conditions for nanopores due to the effective viscosity and slippage with various dimensions and contact angles. The enhancement increases with the diameter and decreases with the contact angle. These results elucidate the confined movement through nanopores, which can be used to understand the low fracturing fluid recovery of shale reservoir formations.

Acknowledgement

This work was supported by the Natural Science Foundation of China (Grant No. 51504203, 51525404, and 51874250), the National Key and Development Program of China (Grant No. 2017ZX05037-004) and the National Students' Platform for Innovation and Entrepreneurship Training Program of China (Grant No. 201810615007).

Conflict of interest

The authors declare no competing interest.

References

Abgrall, P., Nguyen, N.T. Nanofluidic devices and their applications. Anal. Chem. 2008, 80(7): 2326-2341.

Akbarabadi, M., Saraji, S., Piri, M., et al. Nano-scale experimental investigation of in-situ wettability and spontaneous imbibition in ultra-tight reservoir rocks. Adv. Water Resour. 2017, 107: 160-179.

Alkouh, A. New advances in shale gas reservoir analysis using water flowback data. Texas A&M University, Texas, American, 2014.

Benavente, D., Lock, P., Cura, M.A.G.D., et al. Predicting the capillary imbibition of porous rocks from microstructure. Trans. Porous Media 2002, 49(1): 59-76.

Birdsell, D.T., Rajaram, H., Dempsey, D., et al. Hydraulic fracturing fluid migration in the subsurface: A review and expanded modeling results. Water Resour. Res. 2015, 51(9): 7159-7188.

Bocquet, L., Tabeling, P. Physics and technological aspects of nanofluidics. Lab. Chip 2014, 14(17): 3143-3158.

Cai, J., Hu, X., Standnes, D.C., et al. An analytical model for spontaneous imbibition in fractal porous media including

gravity. Colloids Surf. A: Physicochem. Eng. Asp. 2012, 414: 228-233.

Cai, J., Perfect, E., Cheng, C., et al. Generalized modeling of spontaneous imbibition based on Hagen-Poiseuille flow in tortuous capillaries with variably shaped apertures. Langmuir 2014, 30(18): 5142-5151.

Chan, D., Horn, R.G. The drainage of thin liquid films between solid surfaces. J. Chem. Phys. 1985, 83(10): 5311-5324.

Cipolla, C.L. Modeling production and evaluating fracture performance in unconventional gas reservoirs. J. Petrol. Technol. 2009, 61(9): 84-90.

Cottin-Bizonne, C., Barrat, J.L., Bocquet, L., et al. Low-friction flows of liquid at nanopatterned interfaces. Nat. Mater. 2003, 2(4): 237-240.

Dimitrov, D.I., Milchev, A., Binder, K. Capillary rise in nanopores: molecular dynamics evidence for the Lucas-Washburn equation. Phys. Rev. Lett. 2007, 99(5): 054501.

Din, X., Michaelides, E.E. Kinetic theory and molecular dynamics simulations of microscopic flows. Phys. Fluids 1997, 9(12): 3915-3925.

Falk, K., Coasne, B., Pellenq, R., et al. Subcontinuum mass transport of condensed hydrocarbons in nanoporous media. Nat. Commun. 2015, 6: 6949.

Feibelman, P.J. Viscosity of ultrathin water films confined between aluminol surfaces of kaolinite: ab initio simulations. J. Chem. Phys. 2013, 117(12): 6088-6095.

Fradin, C., Braslau, A., Luzet, D., et al. Reduction in the surface energy of liquid interfaces at short length scales. Nature 2000, 403(6772): 871-874.

Ghanbari, E., Dehghanpour, H. The fate of fracturing water: A field and simulation study. Fuel 2016, 163: 282-294.

Granick, S. Motions and relaxations of confined liquids. Science 1991, 253(5026): 1374-1379.

Granick, S., Zhu, Y., Lee, H. Slippery questions about complex fluids flowing past solids. Nat. Mater. 2003, 2: 221-227.

Haria, N.R., Grest, G.S., Lorenz, C.D. Viscosity of nanoconfined water between hydroxyl basal surfaces of kaolinite: classical simulation results. J. Chem. Phys. C 2012, 17(12): 6096–6104.

Heinbuch, U., Fischer, J. Liquid flow in pores: Slip, no-slip, or multilayer sticking. Phys. Rev. A 1989, 40(2): 1144.

Herington, E.F.G. Recommended reference materials for realization of physicochemical properties. Oxford, UK, Pergamon Press, 1977.

Holt, J.K., Park, H.G., Wang, Y., et al. Fast mass transport through sub-2-nanometer carbon nanotubes. Science 2006, 312(5776): 1034-1037.

Hsu, S.Y., Tsai, J.P., Chang, L.C. Pore-scale study of the effect of the saturation history on fluid saturation and relative permeability of three-fluid flow in porous media. Paper Presented at the AGU Fall Meeting Abstracts, San Francisco, American, December, 2014.

Huang, D.M., Sendner, C., Horinek, D., et al. Water slippage versus contact angle: A quasiuniversal relationship. Phys. Rev. Lett. 2008, 101(22): 226101.

Kalyon, D.M. Apparent slip and viscoplasticity of concentrated suspensions. J. Rheol. 2005, 49(3): 621-640.

Kannam, S.K. Todd, B.D., Hansen, J.S., et al. Slip flow in graphene nanochannels. J. Chem. Phys. 2011, 135(14): 144701.

Klein, J., Kumacheva, E. Confinement-induced phase transitions in simple liquids. Science 1995, 269(5225): 816-819.

Laliberté, M. Model for calculating the viscosity of aqueous solutions. J. Chem. Eng. Data 2007, 52(2): 321-335.

Li, T., Gao, J., Szoszkiewicz, R., et al. Structured and viscous water in subnanometer gaps. Phys. Rev. B 2007, 75(11): 115415.

Liu, H., Cao, G. Effectiveness of the Young-Laplace equation at nanoscale. Sci. Rep. 2016, 6: 23936.

Lucas, R. Rate of capillary ascension of liquids. Kolloid-Zeitschrift 1918, 23(1): 15-22.

Loucks, R.G., Reed, R.M., Ruppel, S.C., et al. Spectrum of pore types and networks in mudrocks and a descriptive classification for matrix-related mudrock pores. AAPG Bull. 2012, 96(6): 1071-1098.

Lorenz, U.J., Zewail, A.H. Observing liquid flow in nanotubes by 4D electron microscopy. Science 2014, 344(6191): 1496-1500.

Maali, A., Cohen-Bouhacina, T., Kellay, H. Measurement of the slip length of water flow on graphite surface. Appl. Phys. Lett. 2008, 92(5): 053101.

Mashl, R.J., Joseph, S., Aluru, N.R., et al. Anomalously immobilized water: A new water phase induced by confinement in nanotubes. Nano Lett. 2003, 3(5): 589-592.

Mortensen, N.A., Okkels, F., Bruus, H. Reexamination of Hagen-Poiseuille flow: Shape dependence of the hydraulic resistance in microchannels. Phys. Rev. E 2005, 71(5): 057301.

Müller, M., Pastorino, C., Servantie, J. Flow, slippage and a hydrodynamic boundary condition of polymers at surfaces. J. Phys.: Condens. Matter 2008, 20(49): 494225.

Nair, R.R., Wu, H., Jayaram, P.N., et al. Unimpeded permeation of water through helium-leak-tight graphene-based membranes. Science 2012, 335(6067): 442-444.

Ortiz-Young, D., Chiu, H.C., Kim, S., et al. The interplay between apparent viscosity and wettability in nanoconfined water. Nat. Commun. 2013, 4: 2482.

Petravic, J., Harrowell, P. Spatial dependence of viscosity and thermal conductivity through a planar interface. J. Phys. Chem. B 2009, 113(7): 2059-2065.

Raviv, U., Laurat, P., Klein, J. Fluidity of water confined to subnanometre films. Nature 2001, 413(6851): 51-54.

Ruppert, L.F., Sakurovs, R., Blach, T.P., et al. A usans/sans study of the accessibility of pores in the barnett shale to methane and water. Energ. Fuels 2013, 27(2): 772-779.

Salwen, H., Cotton, F.W., Grosch, C.E. Linear stability of Poiseuille flow in a circular pipe. J. Fluid Mech. 1980, 98(2): 273-284.

Scatena, L.F., Brown, M.G., Richmond, G.L. Water at hydrophobic surfaces: weak hydrogen bonding and strong orientation effects. Science 2001, 292(5118): 908-912.

Schmid, K.S., Alyafei, N., Geiger, S., et al. Analytical solutions for spontaneous imbibition: Fractional-flow

theory and experimental analysis. SPE J. 2016, 21(6): 2308-2316.

Sedghi, M., Piri, M., Goual, L. Molecular dynamics of wetting layer formation and forced water invasion in angular nanopores with mixed wettability. J. Chem. Phys. 2014, 141(19): 194703.

Shaat, M. Viscosity of water interfaces with hydrophobic nanopores: application to water flow in carbon nanotubes. Langmuir 2017, 33(44): 12814-12819.

Shah, D.O. Thin liquid films and boundary layers: special discussion of the faraday society. AIChE J. 1973, 19(6): 1283-1283.

Shannon, M.A., Bohn, P.W., Elimelech, M., et al. Science and technology for water purification in the coming decades. Nature 2008, 452(7185): 301-310.

Sofos, F., Karakasidis, T.E., Liakopoulos, A. Surface wettability effects on flow in rough wall nanochannels. Microfluid. Nanofluid. 2012, 12(1): 25-31.

Thomas, J.A., McGaughey, A.J.H. Density, distribution, and orientation of water molecules inside and outside carbon nanotubes. J. Chem. Phys. 2008a, 128(8): 084715.

Thomas, J.A., McGaughey, A.J.H. Reassessing fast water transport through carbon nanotubes. Nano Lett. 2008b, 8(9): 2788-2793.

Thomas, J.A., McGaughey, A.J.H. Water flow in carbon nanotubes: transition to subcontinuum transport. Phys. Rev. Lett. 2009, 102(18): 184502.

Thompson, P.A., Robbins, M.O. Origin of stick-slip motion in boundary lubrication. Science 1990, 250(4982): 792-794.

Thompson, P.A., Troian, S.M. A general boundary condition for liquid flow at solid surfaces. Nature 1997, 389(6649): 360-362.

Vinogradova, O.I., Koynov, K., Best, A., et al. Direct measurements of hydrophobic slippage using double-focus fluorescence cross-correlation. Phys. Rev. Lett. 2009, 102(11): 118302.

Voronov, R.S., Papavassiliou, D.V., Lee, L.L. Boundary slip and wetting properties of interfaces: Correlation of the contact angle with the slip length. J. Chem. Phys. 2006, 124(20): 204701.

Wang, J., Rahman, S.S. Investigation of water leakoff considering the component variation and gas entrapment in shale during hydraulic-fracturing stimulation. SPE Reserv. Eval. Eng. 2016, 19(3): 511-519.

Washburn, E.W. The dynamics of capillary flow. Phys. Rev. 1921, 17(9): 273-283.

Werder, T., Walther, J.H., Jaffe, R.L., et al. Molecular dynamics simulation of contact angles of water droplets in carbon nanotubes. Nano Lett. 2001, 1(12): 697-702.

Wu, K., Chen, Z., Li, J., et al. Wettability effect on nanoconfined water flow. Proc. Natl. Acad. Sci. USA 2017, 114(13): 3358-3363.

Xiao, J., Cai, J., Xu, J. Saturated imbibition under the influence of gravity and geometry. J. Colloid Interf. Sci. 2018, 521: 226-231.

Yang, L., Yao, T., Tai, Y. The marching velocity of the capillary meniscus in a microchannel. J. Micromech. Microeng. 2004, 14(2): 220-225.

Zeng, F., Guo, J. Optimized design and use of induced complex fractures in horizontal wellbores of tight gas reservoirs. Rock Mech. Rock Eng. 2016, 49(4): 1411-1423.

Zeng, F., Guo, J., Ma, S., et al. 3D observations of the hydraulic fracturing process for a model non-cemented horizontal well under true triaxial conditions using an X-ray CT imaging technique. J. Nat. Gas Sci. Eng. 2018, 52: 128-140.

Zhang, S., Sheng, J. Study of the propagation of hydration-induced fractures in mancos shale using computerized tomography. Int. J. Rock Mech. Min. Sci. 2017, 95: 1-7.

Zhang, X., Morrow, N.R., Ma, S. Experimental verification of a modified scaling group for spontaneous imbibition. SPE Reserv. Eng. 1996, 11(4): 280-285.